Resolving the 1906 M_w 7.1 Meishan, Taiwan, Earthquake from Historical Seismic Records

by Yi-Wun Liao, Kuo-Fong Ma, Ming-Che Hsieh, Shi-Nan Cheng, Hao Kuo-Chen, and Chung-Pai Chang

ABSTRACT

The 1906 M_w 7.1 Meishan earthquake, named after the village near where it occurred, was one of the most damaging earthquakes in Taiwan in the early twentieth century. The historical literature and former studies claimed to show that this earthquake was related to the Meishan fault, which had about 12.5 km right-lateral surface rupture orientated in an east–west direction. However, the surface rupture is short with respect to the magnitude of the earthquake. The north–south pattern of damage is not consistent with the strike of the surface rupture. These apparent inconsistencies raised severe doubts regarding the exact mechanism of the earthquake. Using the original Omori records of the 1906 Meishan earthquake from the historical Taipei, Taichung, and Tainan stations, we carried out an effective waveform simulation to evaluate several different geological fault models. Synthetic Omori records from these geological fault models clearly show a discrepancy in the first motions of *P* and *S* waves at the Tainan station, which suggest that the focal mechanism may not be a pure strike slip. We used observed *P*- and *S*-wave first motions in the historical Omori records as a constraint and performed a grid search to find possible focal mechanisms. The preferred focal mechanism is an oblique thrust fault oriented in the northeast–southwest direction, with a small right-lateral component. Such a focal mechanism not only reproduces the general feature shown in the observed intensity map, it is also more consistent with the spatial distribution of significant aftershocks, which are predominantly located toward the north and south of the epicenter. This result highlights the importance of historical recordings in resolving the earthquake mechanism in a complex fault system.

Electronic Supplement: Figures of *P*- and *S*-wave polarities, simulated intensity maps, and simulated and observed seismograms, and table of parameters of the instrument responses from Omori's and Gray–Milne seismographs for the ancient stations.

INTRODUCTION

The 1906 Meishan earthquake, one of the most damaging earthquakes in Taiwan's history, occurred in the southwestern Taiwan at local time 6:43 a.m. on 17 March. It is located at 23.550° latitude, 120.450° longitude, and 6 km depth (Yeh *et al.*, 1998; Fig. 1). The magnitude of this earthquake was M_H 7.1, first determined by Hsu (1980a,b), and M_s 6.8, subsequently determined by Abe and Noguchi (1983). This earthquake caused 1258 deaths, 2385 injuries, and leveled 6769 houses. According to the Omori (1907) field investigation and the historical literature (Taiwan Governor-General Office of Civil Affairs, 1907; Kondo, 1906), a right-lateral surface rupture with a length of about 12.5 km, identified as the Meishan fault, and liquefactions were observed along the east–west direction (Fig. 2). Thus, the 1906 Meishan earthquake had long been considered as a significant event from the Meishan fault with an east–west strike-slip focal mechanism.

However, the length of the fault is disproportionally short compared to the damage caused by this M_w 7.1 earthquake. The intensity maps compiled by government agencies (Fig. 3a,b,d) show a general north–south pattern, rather than the east–west intensity pattern reported by Omori (1907; see also Fig. 3c). Significant aftershocks were also located to the north and south of the epicenter (Fig. 1). These inconsistent observations had raised long-standing debates regarding the understanding of this devastating historical earthquake.

In 1906, Taiwan was administered as colony by the Japanese government which installed four seismic stations (Fig. 1) over the main island of Taiwan (TAP, TCU, and TAN) and a small island of Penghu (PNG) with the Omori instrument and Gray–Milne seismograph. It was fortunate that valuable seismograms recorded by these stations were discovered in the earthquake data archive project conducted by the Earthquake Research Institute of Tokyo University (Noguchi *et al.*, 2001). These well-preserved historical waveforms allow us to use

doi: 10.1785/0220170285

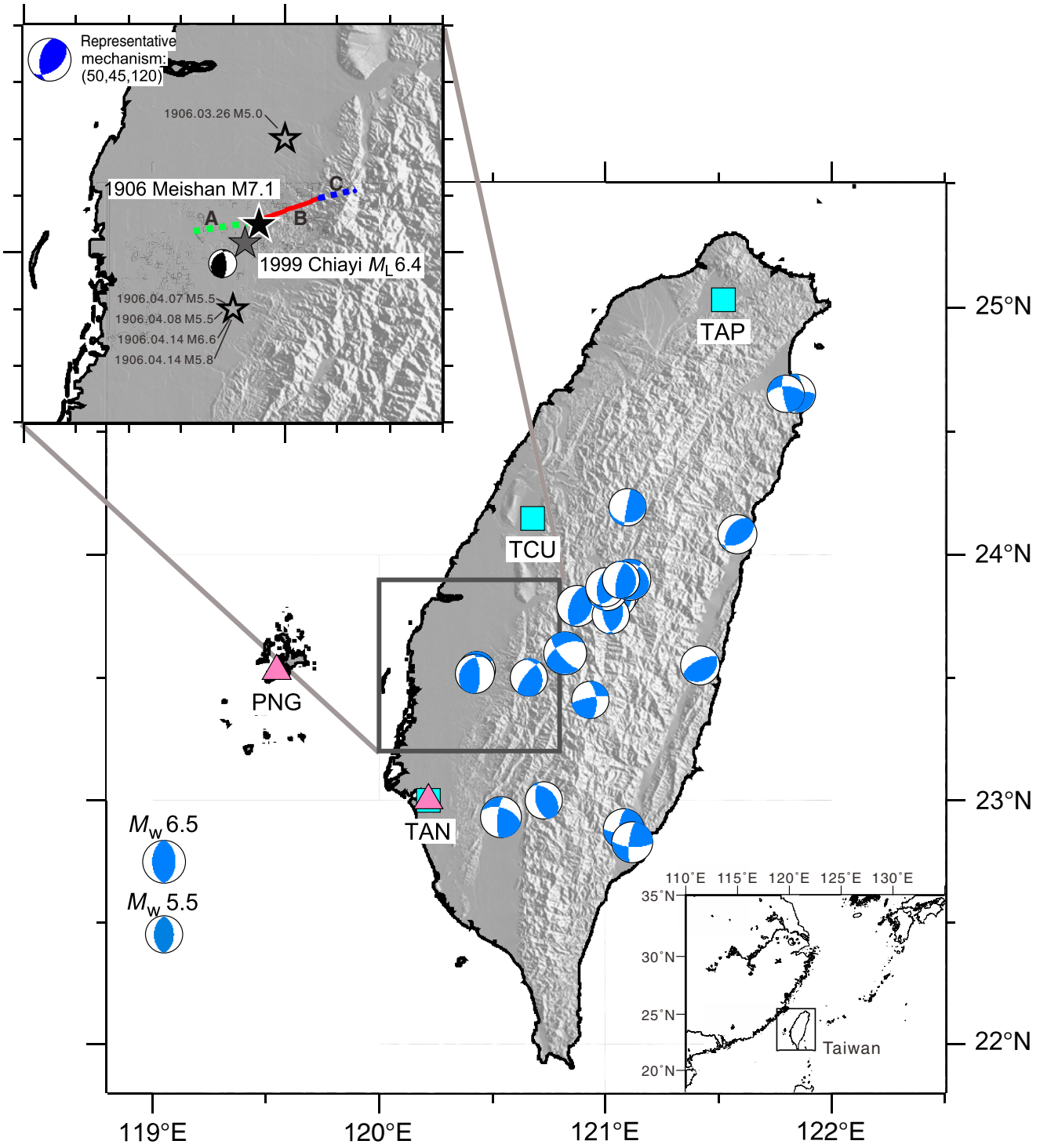

▲ **Figure 1.** The distribution of historical stations with available seismograms from the 1906 Meishan earthquake. The focal mechanisms of inland earthquakes of Taiwan with magnitude larger than M_w 6.5 from 1996 to 2016 from Broadband Array in Taiwan for Seismology are also shown. Squares and triangles indicate the historical stations equipped with one-component Omori seismograph and three-component Gray–Milne seismograph, respectively. The enlarged figure shows the locations of the epicenters of the 1906 Meishan mainshock (black star) and aftershocks (open star) from Sinotech Engineering Consultants, Inc. (1985). The representative focal mechanism derived in this study for the 1906 Meishan earthquake is shown in the upper left corner with strike, dip, and rake. The selected event of the 1999 Chiayi earthquake (gray star) for focal mechanism examination is also shown. The possible fault segments associated with the 1906 Meishan earthquake of segments A (light dashed line), B (solid line), and C (dark dashed line) suggested by Y. H. Lee (personal comm., 2014) are also shown, respectively. The segment B is the segment with observed surface rupture addressed by Omori (1907). The regional map of Taiwan is presented in lower right corner for reference. The color version of this figure is available only in the electronic edition.

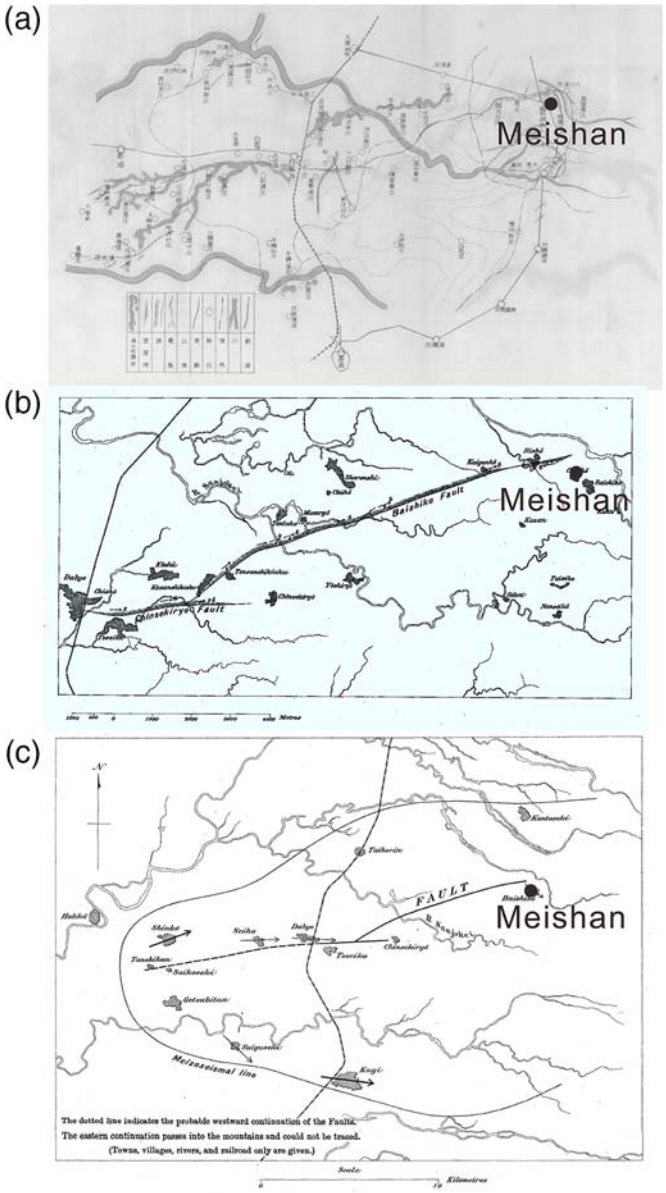

▲ **Figure 2.** The associated surface ruptures of the 1906 Meishan earthquake depicted by the geological survey and documented by government agency in 1906. The village Meishan is denoted by the dot. (a) The report of the 1906 Meishan earthquake from Taiwan Governor-General Office of Civil Affairs (1907). The lines represent the surface ruptures, railways, rivers, and liquefaction. (b) The zoom-in map of (c) showing the surface ruptures and the possible westward extension (dashed line) of the fault suggested by Omori (1907). The shade zone next to the surface rupture in (b) represented the downward side, and the arrows indicate the slip direction observed in the field. The color version of this figure is available only in the electronic edition.

modern waveform simulations to decipher the mechanism of the 1906 Meishan earthquake.

In this study, two types of simulations were performed. First, we computed ground motions based on fault models from geological investigations (e.g., Lee and Shih, 2011) to synthesize Omori waveforms at three stations (TAP, TCU, and TAN) and intensity maps. Second, we use the polarities of the historical Omori seismograms as constraints to obtain a representative focal mechanism, which has high-angle reverse faulting. We will show that the derived composite fault model of this high-angle reverse faulting with the surface rupture segment of Meishan fault will reproduce a damage pattern and aftershock distribution more consistent with observations.

HISTORICAL RECORDS

There were two types of instruments installed at these historical seismic stations, including a single east–west-component Omori instrument at stations TAP, TCU, and TAN, and a three-component Gray–Milne seismograph at stations PNG and TAN. Figure 4 shows the historical records with sketched traces associated with the 1906 Meishan earthquake. Because the timescale for Gray–Milne seismographs is unclear, we first focus on the three stations with the Omori records. We identified the possible *P*- and *S*-wave arrivals, measured the *S*–*P* times, and marked the lasting times from *P*-wave arrival to the time that the records were clipped (as shown in Fig. 4) for reference.

We compiled instrument parameters of the Omori seismograph and the Gray–Milne seismograph. The magnifications of Omori seismograph are 10, 6, and 6 for stations TAP, TCU, and TAN, respectively, according to the document of Taihoku Meteorological Observatory (TMO, 1911). The period and damping factor for Omori's seismograph were considered to be 12 s and 0.2 (TMO, 1911; Kanamori *et al.*, 2012). For the Gray–Milne seismograph, the magnifications were 5 for the east–west and north–south components and 10 for the up–down component, and the period and damping factor were 3 s and 0.1 (TMO, 1911; Fukuyama *et al.*, 2007).

We performed numerical simulation with the developed fault models and convolved synthetic waveforms with the instrument parameters to simulate synthetic Omori and Gray–Milne seismograms. Because historical Omori records have been more widely examined through previous studies, for example, 1909 Taipei earthquake (Kanamori *et al.*, 2012), we emphasize more on the comparison with the Omori records than the Gray–Milne records. Although teleseismic records from this damaging earthquake might be potentially available, we focused on accessible records at local historical stations and did not reach out for data recorded at teleseismic stations.

HISTORICAL SEISMOGRAMS AND INTENSITY SYNTHESIS

Simulation Based on the Geological Fault Models

According to historical documents and further investigation from Global Positioning System and field data (Lee and Shih, 2011), Y. H. Lee (personal comm., 2014) suggested three fault segments possibly associated with the Meishan earthquake. Segments A–C are associated with the extent of liquefaction, the main surface rupture (Omori, 1907), and a possible blind fault

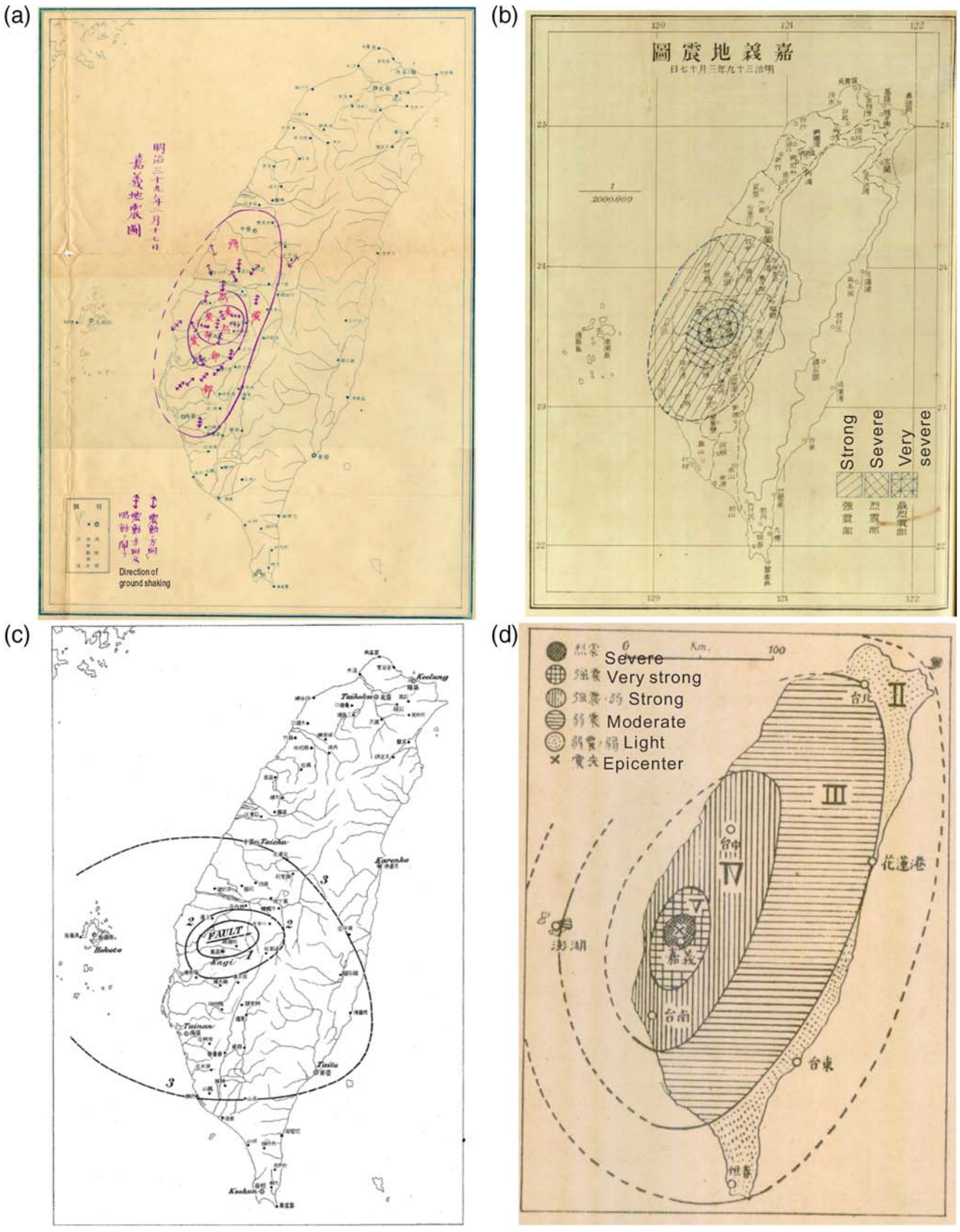

▲ **Figure 3.** Historical intensity maps from (a) the report of the 1906 Meishan earthquake, (b) the Taiwan Governor-General Office of Civil Affairs (1907), (c) Omori (1907), and (d) TMO (1936). The intensity scales represented in the individual maps are also shown with English translation. The color version of this figure is available only in the electronic edition.

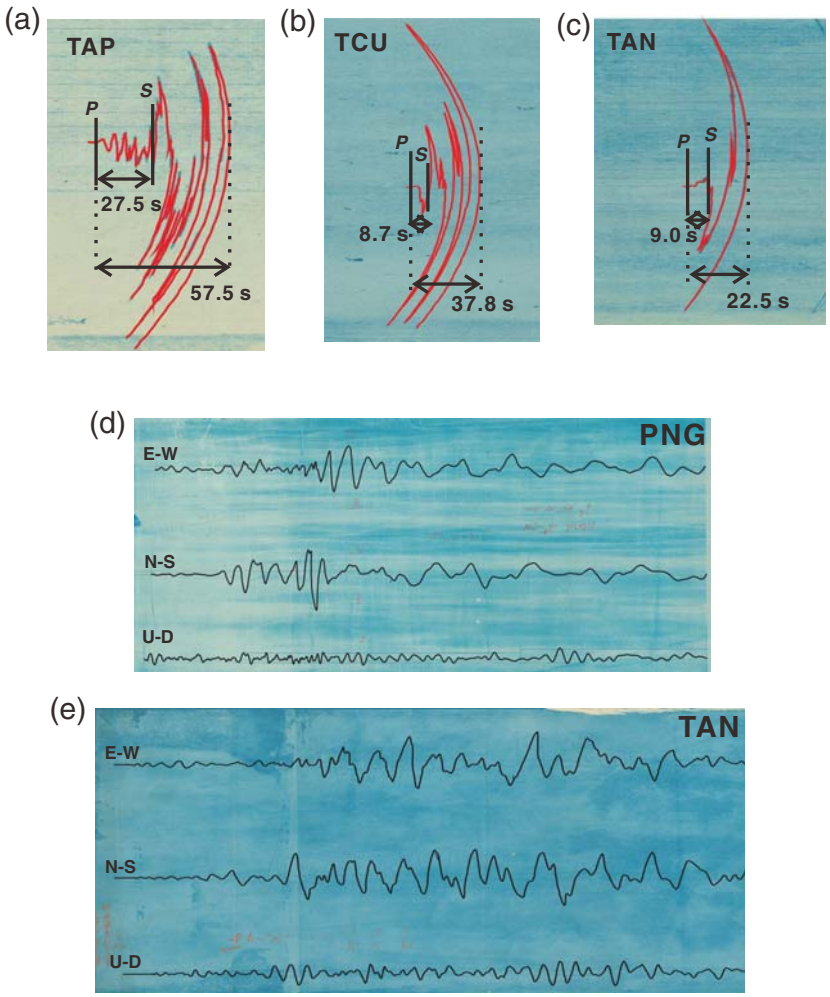

▲ **Figure 4.** The historical records of the 1906 Meishan earthquake. The traces were sketched with solid lines. (a–c) The records of east–west (E-W) Omori seismograph at the stations TAP, TCU, and TAN, respectively. The records were interrupted by the large amplitudes after arrival of *S* wave. The *P*- and *S*-wave arrivals were identified with vertical lines. The relative *S*–*P* times at each station were also marked, and the time from *P*-wave arrival to the available waveforms was also marked, despite the distortion of the waveforms from the pen curvature. (d,e) The three-component (E-W, north–south [N-S], and up–down [U-D]) records of Gray–Milne seismograph at the stations PNG and TAN, respectively. The color version of this figure is available only in the electronic edition.

segment toward the mountain range (see also Fig. 1), respectively. The strikes of segments A–C are 84°, 75°, and 75° (Y. H. Lee, personal comm., 2014), respectively, and all three segments have the same dipping angle of 75° to the south and fault width extended to the seismogenic depth of 15.5 km. Because there is no available information on the rake angles of the three segments, we use the rake angle of 153° from S.-N. Cheng (personal comm., 2014; see also Data and Resources).

Because segment B is mapped with surface rupture, we used the segment B as the main segment and considered three possible combinations of the fault segments to calculate synthetic seismograms. Fault model I uses only the main segment B, with a length of 12.5 km and a width of 15.5 km. We scale the fault length to the magnitude and the amount of slip (Wells and Coppersmith, 1994) and estimated M_w of 6.3 and an average slip of 244 cm. Fault model II combines fault segments B and C. The length of the fault is 19.5 km, the width is 15.5 km, as above, and the corresponding M_w is 6.5, with an average slip of 303 cm. Fault model III combines fault segments A–C. The length of the fault is 32.7 km, the width is 15.5 km, and the corresponding M_w is 6.7, with an average slip of 350 cm. We subsequently implemented these fault models in the finite-fault modeling assuming a uniform slip distribution.

In the finite-fault modeling (Hsieh *et al.*, 2014), the fault planes were divided into subfaults of 2 km × 2 km, and fault models I–III have 48, 77, and 133 subfaults, respectively (Fig. 5). We considered the location from Yeh *et al.* (1998) as the starting point of the rupture in each fault model. The rupture speed is assumed at 2.5 km/s, which is about 80% of the shear-wave velocity at the hypocentral depth (Kuo-Chen *et al.*, 2012).

To compute realistic ground motion, we used the strain Green's tensor (SGT) method of Zhao *et al.* (2006) and the SGT database developed by Hsieh *et al.* (2014) to account for the effect of 3D velocity structure (Kuo-Chen *et al.*, 2012) and topography (ETOPO1; Amante and Eakins, 2009). The horizontal grid spacing at the surface of the SGT database is 4 km and the subsurface grid points have uniform horizontal spacing of 2.4 km and vertical spacing ranging from 0.857 km near the surface to 3.913 km at a depth of 40 km (Hsieh *et al.*, 2014). The source time function is a Gaussian function with a characteristic width of 2 s, which yields waveforms with a maximum frequency of 0.8 Hz. With the SGT database, the simulation can be done within a few minutes, making it feasible to conduct a systematic grid search.

Because the observed waveforms were recorded by an Omori seismograph with a single east–west component, we convolved the synthetic waveforms in the east–west component with the instrument responses to obtain simulated Omori records at stations TAP, TCU, and TAN (Kanamori *et al.*, 2012). Figure 6 compares the observed waveform against simulated Omori records from three fault models in the same timescale. Because the amplitude scale of these historical records was not known, we considered only the polarity and the *S*/*P* amplitude ratio in the following comparison. In general, the predicted *S*–*P* times are in good agreement with the observed ones (Fig. 6). As shown in Figure 6a,b, the predicted polarities of the *P* and *S* waves at stations TAP and TCU also

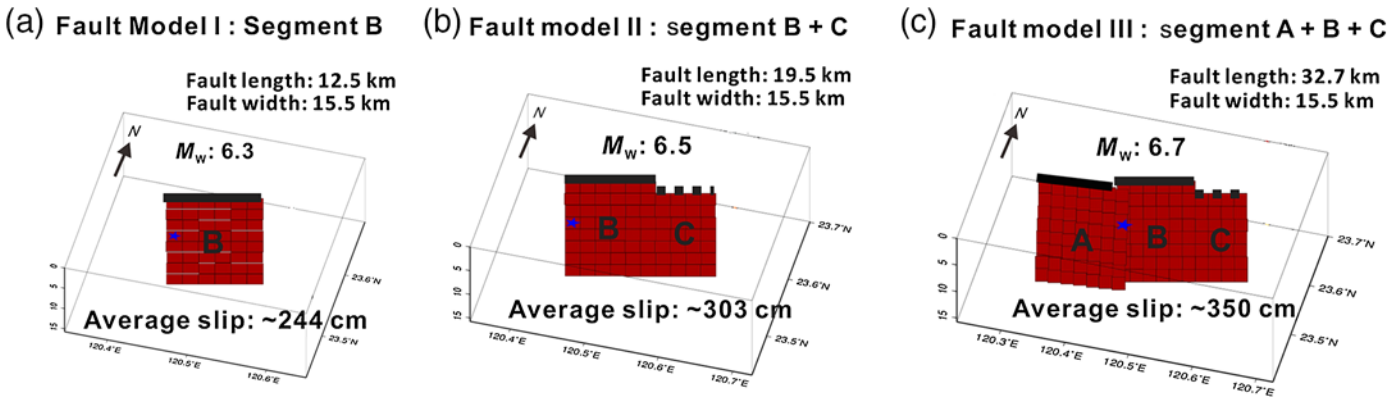

▲ **Figure 5.** Three geological fault models following Y. H. Lee (personal comm., 2014) for the simulation of the finite-fault modeling of the 1906 Meishan earthquake. (a) Fault model I with only the main fault, segment B. (b) Fault model II with the main fault (segment B) and the blind fault (segment C). (c) Fault model III with a western extension of liquefaction zone (segment A), main fault (segment B), and the blind fault (segment C). The corresponding fault lengths and widths in each finite-fault model were shown with homogeneous slip. The corresponding moment magnitude and average slip adopted the scaling law of Wells and Coppersmith (1994). Bold lines and dashed line indicate the fault segment with and without rupture to the surface, respectively. The color version of this figure is available only in the electronic edition.

match the observed *P*- and *S*-wave polarities, showing the upward *P*- and *S*-wave motions. However, the predicted polarities at station TAN (Fig. 6c) showed downward motion in both *P* and *S* waves, which is inconsistent with the upward *P*-wave motion and downward *S*-wave motion observed at this station (Fig. 4c).

Preliminary inspection of the polarities shows a discrepancy for the *P* and *S* waves at station TAN. But the *S*/*P* amplitude ratio at this station is best explained by fault model III, suggesting that a fault dimension of about 33 km might be necessary to reproduce the strong *S* wave observed at station TAN and reconcile the large magnitude of 7.1 reported in the historical documents.

In our synthesis, the frequency content of the synthetic waveforms is up to 0.8 Hz, which might not be sufficiently high to reproduce the frequency content in the ground acceleration. Therefore, instead of mapping the intensity directly from peak ground acceleration (PGA), we derived the synthetic intensity map through the scaling between PGA and peak ground velocity established by Wu *et al.* (2003). Figure 6d–f shows the converted synthetic intensity maps of fault models I–III, respectively. Because of the directivity along the east–west-oriented fault segments, high-intensity pattern trends in the east–west direction, which is inconsistent with the observed intensity maps of high-intensity pattern trending in the north–south direction (Fig. 3). This discrepancy indicates that the fault system associated with the 1906 Meishan earthquake may not be limited to the extent of surface rupture along a strike-slip fault (segment B). The inconsistency in the polarity of the *P* and *S* waves at station TAN also suggests that additional fault segments with a different geometry and slip direction might be needed to explain both the historical records and the intensity map.

Grid Search in Focal Mechanism for the 1906 Meishan Earthquake

To explore alternative focal mechanisms for the 1906 Meishan earthquake, we use the observed *P*- and *S*-wave polarities from the Omori records at stations TAP, TCU, and TAN as constraints. On the basis of the focal mechanism previously determined by S.-N. Cheng (personal comm., 2014), we grid-searched the source parameters of strike, dip, and rake in 15° increments in the 45°–105°, 0°–90°, and 60°–150° ranges, respectively. Because the *S*/*P* amplitude ratio at station TAN is well reproduced by fault model III (Fig. 6c), we considered the length of fault model III as the fault length used in conducting the grid search. Using the SGT method and database, we computed synthetic waveforms for a total number of 245 fault models with different focal mechanisms. The epicenter location from Yeh *et al.* (1998) is adopted as the starting point of the rupture in each fault plane and placed at the center of each fault model. Other parameters such as subfault size, rupture speed, and slip distribution on fault plane are the same as those used in fault model III. Finally, we convolved all synthetic waveforms with the instrument response of the Omori's seismograph to simulate Omori records at stations TAP, TCU, and TAN. The predicted *P*- and *S*-wave polarities in the east–west component were identified from these simulated Omori records and displayed in Ⓔ Figure S1 (available in the electronic supplement to this article). About 18 out of 245 focal mechanisms that can explain the observed polarities of all three stations were selected as potential candidates for the 1906 Meishan earthquake.

Additionally, we compared the synthetic intensity maps of the 18 mechanisms with the observed intensity maps (Ⓔ Fig. S2). Through visual inspection, synthetic intensity maps from two mechanisms, M0081 and M0082, resemble the observed intensity maps the best. These two mechanisms share common source parameters with a strike of 60°, a dip of

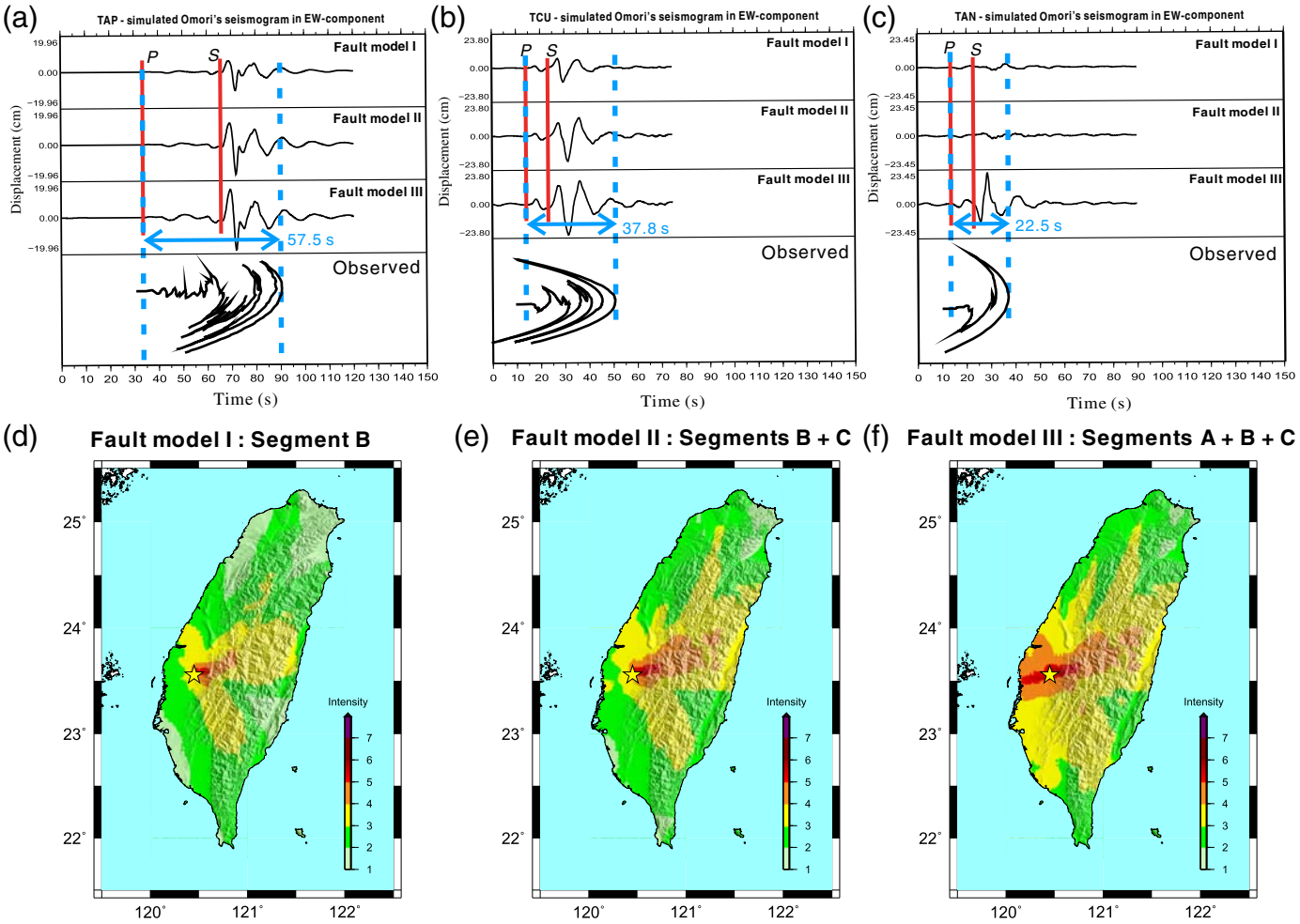

▲ **Figure 6.** The simulated synthetic Omori records of finite-fault models I–III for the stations (a) TAP, (b) TCU, and (c) TAN. The observed records lined up with *P* arrival and with the timescaled to the time of synthetics were placed at the bottom of each station for comparison. The arrivals of *P* and *S* waves were marked with solid vertical lines. The lasting time of the available waveform from *P*-wave arrival in the observed Omori records was denoted and marked with dashed vertical lines. (d–f) The synthetic intensity maps of fault models I–III, respectively. The star represents the epicenter. The color version of this figure is available only in the electronic edition.

60°, and rake angles of 105° and 120°. This result revealed that, despite the east–west-oriented surface rupture along a relatively short strike-slip fault, the 1906 Meishan earthquake might have resulted primarily from a fault geometry structure with a strike trending in the northeast–southwest direction, a high-angle dip of 60°, and a right-lateral thrusting focal mechanism.

The grid search in strike was from 45° to 105° with a 15° increment. Because the strike of 45° cannot explain the polarity in all three stations, we tested the strike of 45°–60° with a 5° increment to further examine the strike that may be also permissible to the polarity data. As a result, a strike of 50° can also explain the polarity data. Thus, the alternative focal mechanisms might be with a strike of 50°–60°, a dip of 30°–60°, and a rake of 105°–120°. As the high-intensity pattern trends toward the north–south direction, we suggest the fault strike of 50° as the representative focal mechanism (Fig. 1), along with other associated parameters as dip = 45° and rake = 120°. Figure 7a shows the simulated Omori records calculated from the representative focal mechanism and the corresponding intensity map. Even though the absolute amplitude of the historical Omori records is uncertain and the recording suffers distortion from the pen curvature, simulated Omori records can explain the polarity data at all three stations as well as the observed *S*/*P* amplitude ratio from these available waveforms.

Because this earthquake produced a surface rupture along the east–west-trending Meishan fault, we further considered a composite fault model that combines the preferred focal mechanism with the east–west-trending Meishan fault (segment B in Fig. 5). Figure 7b shows the simulated Omori records for this composite fault model and the resulting intensity map. The composite fault model yields a magnitude of M_w 6.79. The simulated Omori records from the composite fault model (Fig. 7b) are quite similar to those shown in Figure 7a. However, the amplitude in Figure 7b is not only larger than that in Figure 7a due to an increase in M_w from 6.7 to

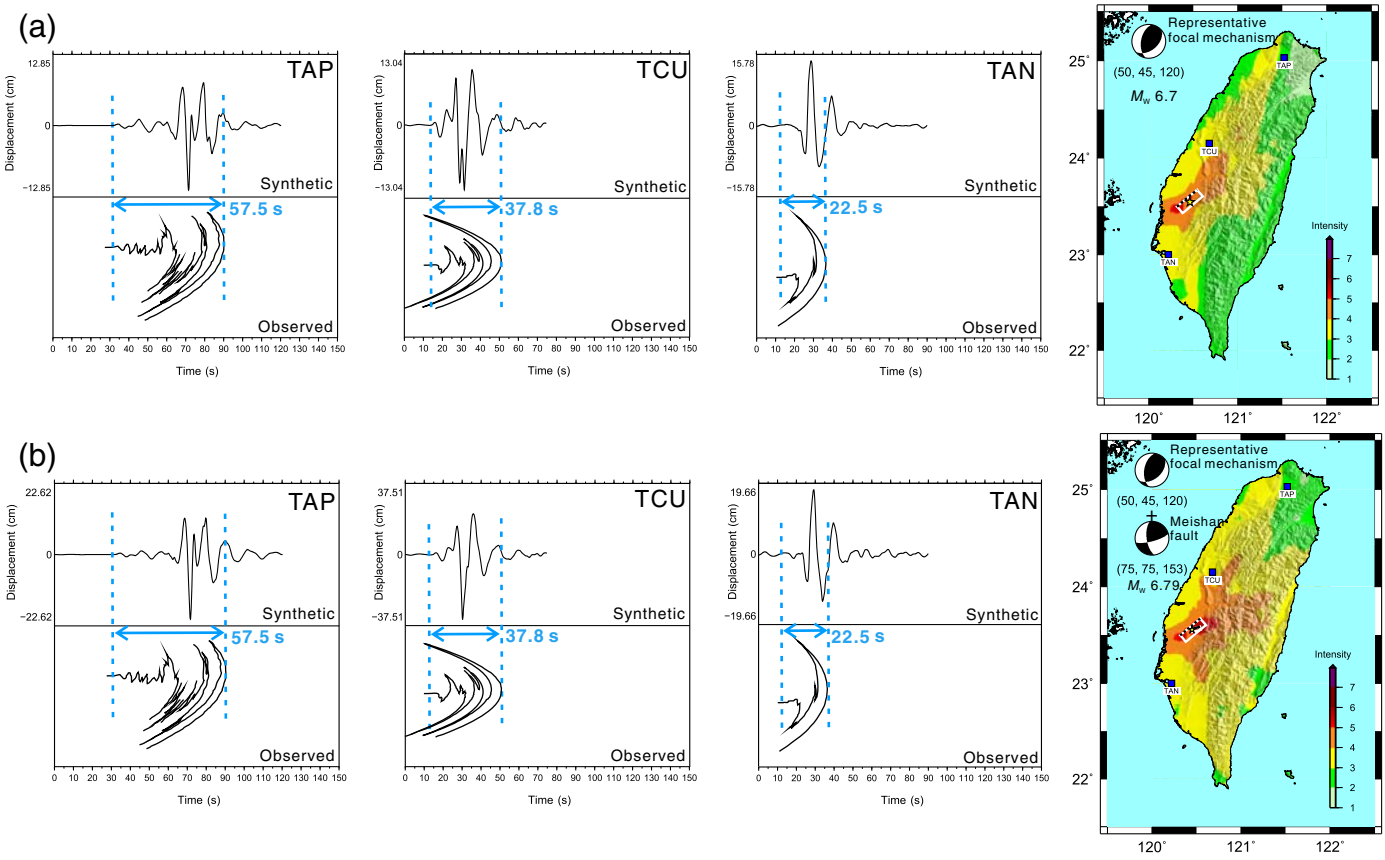

▲ **Figure 7.** The synthetic and observed Omori records in E-W-component and intensity of (a) the fault with the representative focal mechanism and (b) the composite fault model, fault with representative focal mechanism and surface rupture of Meishan fault (segment B, Fig. 5a). The historical Omori records were lined up with synthetic Omori records from *P* arrivals. The lasting of the available waveforms was denoted and marked by dashed lines. For the simulated intensity maps, the star represents the location of the hypocenter, and the rectangles indicate the surface projection of the corresponding fault planes. The focal mechanisms and the corresponding moment magnitudes were placed at the upper left corner with strike, dip, and rake. The color version of this figure is available only in the electronic edition.

6.79, the composite fault model also yields a broader high-intensity pattern because of the addition of the Meishan fault. Through visual inspection, the synthetic intensity map not only compares well with the east–west high-intensity pattern shown by Omori (1907; see also Fig. 3c), but it also reproduces the overall intensity pattern trending in the northeast–southwest direction, consistent with reports by several government agencies in 1906 (Fig. 3a,b,d).

Simulating Historical Gray–Milne Records

Using a representative focal mechanism (strike 50°, dip 45°, and rake 120°), we further simulated historical Gray–Milne records at station TAN (Fig. 8a) and compared them against the observed records. Because the Gray–Milne records are recorded by a long-period instrument, the initial motions of *P* and *S* waves are less distinct than the Omori records. While examining the entire three-component records, our representative focal mechanism cannot explain the amplitude ratios among the three-component Gray–Milne records. In the simulated Gray–Milne records, the peak amplitude in the vertical component is much larger than that in the two horizontal components (Fig. 8a), whereas the historical records show the opposite (Fig. 8d).

To examine the sensitivity of the amplitude ratios among the three components with respect to focal mechanism, we examine synthetics with a fixed strike at 50° and different dip and rake (Fig. 8b,c), respectively. It shows that, even with the changes in dip or rake of 15°, we are unable to explain the amplitude ratios among the three-component Gray–Milne records. We also simulated Gray–Milne records using the original strike-slip focal mechanism of fault model III (Ⓔ Fig. S3), but the amplitude ratios remains similar to those calculated from our representative focal mechanism. As the instrument parameters such as the magnification and damping factor are adopted directly from TMO (1911; see also Ⓔ Table S1), it is possible that the comparison of amplitude ratios among three components could be misleading due to inadequate magnification factors. Nevertheless, the mismatch in the amplitude ratios, among three-component Gray–Milne records, remains unresolved with the simulations.

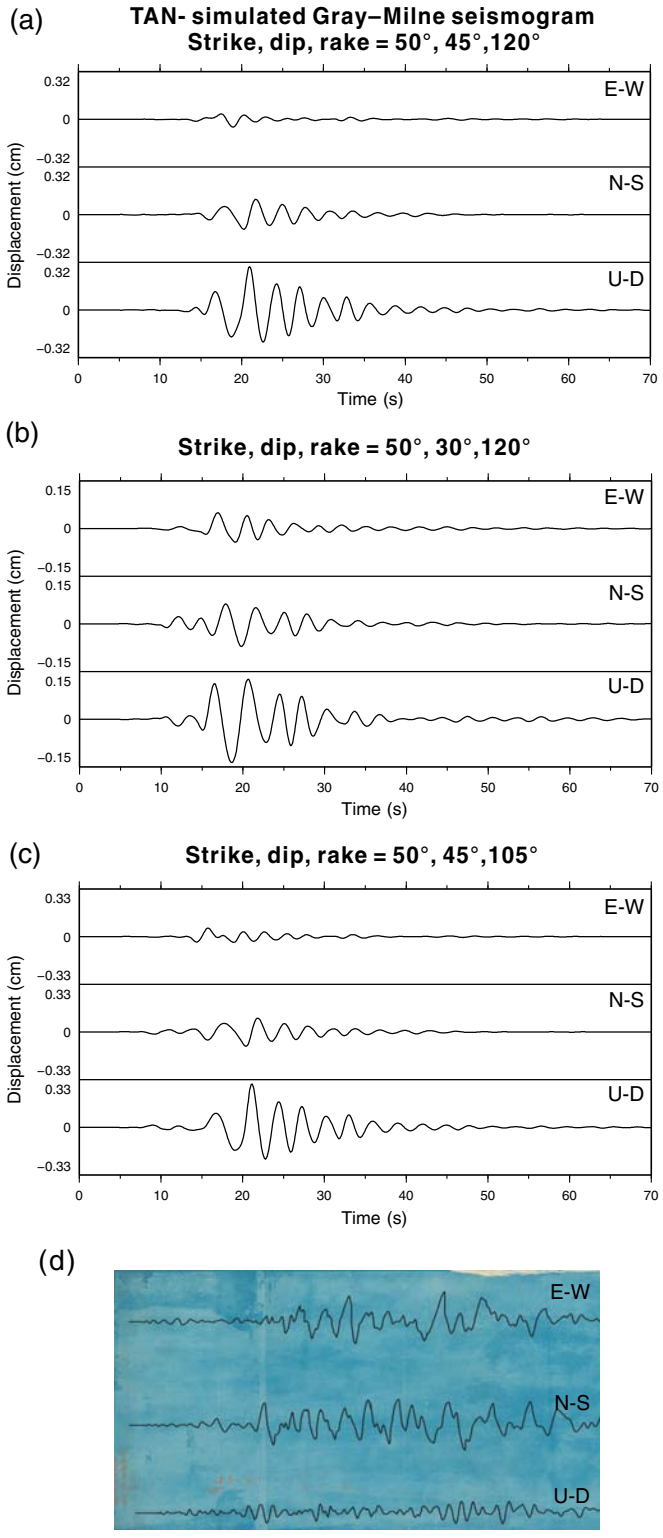

▲ **Figure 8.** The simulated three-component Gray–Milne seismograms of the TAN station using (a) the representative focal mechanism of strike 50°, dip 45°, and rake 120°, (b) the focal mechanism of strike 50°, dip 30°, and rake 120°, and (c) strike 50°, dip 45°, and rake 105°, and (d) the historical three-component Gray–Milne seismograms. The color version of this figure is available only in the electronic edition.

Therefore, to further examine the focal mechanism associated with the 1906 Meishan earthquake, we searched modern records at PNG and TAN stations from earthquakes in southwestern Taiwan to simulate historical Gray–Milne records. Figure 1 shows the distribution of earthquakes with $M_w > 6.5$ since 1996 and their focal mechanisms. Most of the events in southwestern Taiwan have a thrust focal mechanism, similar to our representative mechanism obtained for the 1906 Meishan earthquake (Fig. 1). Among them, we identified the 22 October 1999 M_L 6.4 earthquake in southwestern Taiwan near the source region of 1906 Meishan earthquake for a more detailed comparison. The focal mechanism of this 22 October 1999 event (Fig. 1) shows a thrust focal mechanism with a strike more in the north–south direction. We used strong-motion waveforms recorded at PNG and TAN stations (Taiwan Strong Motion Instrumentation Program; locations similar to that of the 1906 Meishan earthquake) from the 22 October 1999 event to simulate Gray–Milne records. Although the timescale for the PNG and TAN stations for 1906 Gray–Milne records is uncertain (Fig. 4), the simulated Gray–Milne records show similar amplitude in the three components, and it resembles slightly better historical Gray–Milne records of the 1906 Meishan earthquake (Ⓔ Fig. S4).

Tectonic Implication: Northeast–Southwest-Thrust Faulting with an East–West Strike-Slip Surface Rupture

Although the amplitude ratios among three components of historical Gray–Milne records are less well reproduced by our synthetics, the predominant thrust mechanism obtained through analysis of historical Omori records and intensity maps is an important discovery. For nearly a century, the 1906 Meishan earthquake had been considered as a strike-slip event because of the observed surface rupture on the Meishan fault (segment B). However, as discussed above, the enigma lies at the disproportionally short fault length relative to the magnitude of the event, and the spatial pattern of high intensity. The discovery of historical records and the use of modern simulation techniques help us resolve this debate. Further, the study yields a more northeast–southwest thrust faulting mechanism rather than an east–west strike-slip focal mechanism.

In spite of the inconsistency mentioned above, the question regarding the aftershock distribution of the 1906 earthquake had also been raised. Figure 1 shows the distribution of the significant aftershocks of the 1906 Meishan earthquake. With the representative thrust focal mechanism and a strike of 50°, these significant aftershocks are located near the northern and southern portions of the fault. This consistency further validates the likelihood of the resolved mechanism. It is conceivable that this earthquake resulted from a thrust fault system, which was revealed in the southwestern Taiwan by Kuo-Chen *et al.* (2017). The observed east–west strike-slip surface rupture might be part of a composite fault system, but it may not be the driving mechanism for the 1906 Meishan earthquake.

The seismotetonic features of southwestern Taiwan can be associated with two major fault systems—a tensional fault

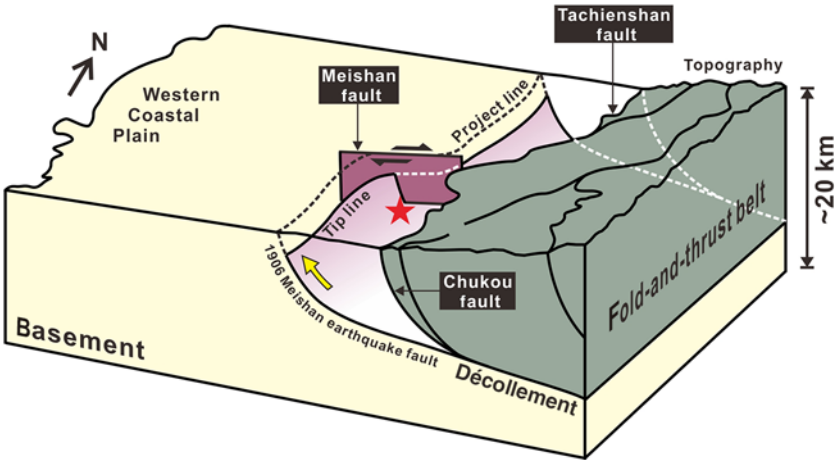

▲ **Figure 9.** The scheme for the geometry of the possible episode for the E-W-striking surface rupture between two N-S thrust faults. The star represents the hypocenter of the 1906 Meishan earthquake. The color version of this figure is available only in the electronic edition.

system with a strike orientating nearly east–west and a fold-and-thrust belt with a strike orientating nearly north–south, resulting from two separate tectonic episodes (Brown *et al.*, 2017). The normal-fault system was associated with the rifted passive continental margin during the Miocene. Currently, some faults within this fault system are reactivated because of the collision between the Eurasian and Philippine Sea plates. The Meishan fault with a high dip angle is considered as one of those faults in our study area. On the other hand, the fold-and-thrust belt was created by the current mountain-building process; for example, the Chiayi blind thrust belongs to this system. Based on the results of ambient noise tomography, the Chiayi blind thrust has been cut through by the reactivated dextral Meishan fault (C. Y. Cheng *et al.*, 2018, unpublished manuscript, see Data and Resources). A thrust focal mechanism obtained from our study could be related to the system in the same way the Chiayi blind thrust relates to the fold-and-thrust belt.

The Meishan fault could be considered as an independent strike-slip fault located in the front of the fold-and-thrust belt of the Taiwan orogeny. In view of the structural evolution, the stress and deformation patterns of the Meishan fault area were driven into the fold-and-thrust belt, which propagates toward the west with a considerable speed as observed in the geodetic data (e.g., Yu *et al.*, 1997; Hu *et al.*, 2001; Hsu *et al.*, 2009). With the progressive evolution, the reverse fault becomes a dominant mechanism in this area. The 1906 Meishan earthquake could be considered an event that marks the reverse focal mechanism and evidences the stress status during the evolution process.

A possible scenario for this evolution is depicted in Figure 9. The 1906 Meishan earthquake occurring along a northeast–southwest-trending reverse fault was not large enough to generate a fault scarp along its own fault plane, but it nonetheless triggered the surface rupture along the pre-existing weak zone of the Meishan fault. Because the Meishan fault is a weak zone that is shallow in depth, it could be easily caught by this reverse fault from a greater depth. The predominantly thrust focal mechanism of the 1906 Meishan earthquake is an important feature with respect to the mitigation of seismic hazard from future earthquakes. Most importantly, the seismic hazard in southwestern Taiwan is not driven by an individual fault segment, but rather it is driven by the fault system.

CONCLUSIONS

We revisited the focal mechanism of the 1906 M_w 7.1 Meishan damaging earthquake using historical Omori records and validated the resolved mechanism against Gray–Milne records. The historical literature suggests that the Meishan earthquake, which had a right-lateral surface rupture orienting in the east–west direction, was related to the Meishan fault. The historically proposed surface rupture is too short for an earthquake having the reported magnitude, and there are inconsistencies between the strike of that surface rupture and the observed patterns of high intensities and aftershocks. Using the Omori records at the historical Taipei, Taichung, and Tainan stations to examine the mechanism of the earthquake, we first carried out waveform simulation of the 1906 Meishan earthquake from geological fault models with an east–west strike and simulated Omori records from modern waveform techniques for comparison. The discrepancy in the first *P*-wave and *S*-wave motions between simulated and observed Omori records at the Tainan station (TAN) calls for the need to consider alternative focal mechanisms. Using observed *P*- and *S*-wave first motions of Omori historical records as constraints, we performed a grid search to determine focal mechanism. As a result, an oblique thrust fault mechanism with a small right-lateral component was revealed. The intensity map predicted by the oblique thrust fault and the Meishan fault provides a rather consistent pattern with the observed intensity maps. The thrust focal mechanism with a strike orienting northeast–southwest also explains the fact that significant aftershocks lay mostly to the northern and southern regions of the mainshock. We demonstrate the importance of historical waveforms in understanding the faulting mechanism of the damaging Meishan earthquake, which involved a complex fault system rather than a single fault segment.

DATA AND RESOURCES

Relevant historical literature and records are archived by Central Weather Bureau (CWB), the database of historical seismograms in Taiwan (http://gdms.cwb.gov.tw/HisEq, last accessed December 2017), and a video by S.-N. Cheng (2014), Echo from the past, Lesson 3: the 1906 Meishan earthquake, available at http://tec.earth.sinica.edu.tw/new_web/video_con

.php?id=5 (last accessed November 2016). The Taiwan Earth Model is available from http://tec.earth.sinica.edu.tw/hisevent/ (last accessed April 2018). The original historical seismograms we used are archived at Earthquake Research Institute (ERI) of Tokyo University at http://wwweic.eri.u-tokyo.ac.jp/record-W/taiwan.html (last accessed February 2018). The strong-motion records of the 22 October 1999 earthquake at stations PNG and TAN were requested from the CWB Geophysical Database Management System (GDMS) system (http://gdms.cwb.gov.tw/, last accessed November 2016). The unpublished manuscript by C. Y., Cheng, H. Kuo-Chen, D. Brown, H. Yao, and K. F. Ma (2018), "Using high-resolution 3D ambient noise tomography to investigate the velocity structure around the Meishan active fault of western Taiwan," submitted to *Tectonophysics*.

ACKNOWLEDGMENTS

The authors would like to thank the Central Weather Bureau for providing the historical earthquake literature and the strong-motion records of modern event. The assistance of Kenji Satake at Earthquake Research Institute of Tokyo University to retrieve the historical Omori records and Gray–Milne records are highly appreciated. The authors also thank the discussion with Hiroo Kanamori at California Institute of Technology, and Teh-Ru Alex Song at University College London during the study. Their work was supported by the Ministry of Science and Technology, Ministry of Science and Technology (MoST) 107-2119-005-011-, Taiwan.

REFERENCES

Abe, K., and S. I. Noguchi (1983). Revision of magnitudes of large shallow earthquakes, 1987-1912, *Phys. Earth Planet. In.* 33,, 11.

Amante, C., and B. W. Eakins (2009). *ETOPO1 1 Arc-Minute Global Relief Model: Procedures, Data Sources and Analysis*, US Department of Commerce, National Oceanic and Atmospheric Administration, National Environmental Satellite, Data, and Information Service, National Geophysical Data Center, Marine Geology and Geophysics Division, Colorado.

Brown, D., J. Alvarez-Marron, C. Biete, H. Kuo-Chen, G. Camanni, and C. W. Ho (2017). How the structural architecture of the Eurasian continental margin affects the structure, seismicity, and topography of the south-central Taiwan fold-and-thrust belt, *Tectonics* **36,** no. 7, 1275–1294.

Fukuyama, E., I. Muramatu, and T. Mikumo (2007). Seismic moment of the 1891 Nobi, Japan earthquake estimated from historical seismograms, *Earth Planets Space* **59,** no. 6, 553–559.

Hsieh, M.-C., L. Zhao, and K.-F. Ma (2014). Efficient waveform inversion for average earthquake rupture in three-dimensional structures, *Geophys. J. Int.* **198,** no. 3, 1279–1292.

Hsu, M.-T. (1980a). *Earthquake Catalog for Taiwan from 1644 to 1979*, Center for Earthquake Engineering Research National Taiwan University, 77 pp.

Hsu, M.-T. (1980b). Destructive earthquakes in Taiwan—From 1644 to the present time, *Meteorol. Bull. Cent. Weather Bur.* **26,** no. 3, 17.

Hsu, Y.-J., S.-B. Yu, M. Simons, L.-C. Kuo, and H.-Y. Chen (2009). Interseismic crustal deformation in the Taiwan plate boundary zone revealed by GPS observations, seismicity, and earthquake focal mechanisms, *Tectonophysics* **479,** no. 1, 4–18.

Hu, J. C., S. B. Yu, J. Angelier, and H. T. Chu (2001). Active deformation of Taiwan from GPS measurements and numerical simulations, *J. Geophys. Res.* **106,** no. B2, 2265–2280.

Kanamori, H., W. H. K. Lee, and K.-F. Ma (2012). The 1909 Taipei earthquake-implication for seismic hazard in Taipei, *Geophys. J. Int.* **191,** no. 1, 126–146, doi: 10.1111/j.1365-246X.2012.05589.x.

Kondo, K. (1906). *Report of the Severe Chiayi Earthquake of March 17, 1906*, 13 pp. (in Japanese).

Kuo-Chen, H., K.-X. Chen, W.-F. Sun, C.-W. Ho, Y.-H. Lee, Z.-K. Guan, C.-C. Kang, and W.-Y. Chang (2017). 3D vs ambient noise tomography in the source region of the 2016 M_w 6.4 Meinong earthquake in Taiwan, *Terr. Atmos. Ocean. Sci.* **28,** no. 5, 693–701.

Kuo-Chen, H., F. T. Wu, and S. W. Roecker (2012). Three-dimensional P velocity structures of the lithosphere beneath Taiwan from the analysis of TAIGER and related seismic datasets, *J. Geophys. Res.* **117,** no. B6, doi: 10.1029/2011JB009108.

Lee, Y. H., and Y. X. Shih (2011). Coseismic displacement, bilateral rupture, and structural characteristics at the southern end of the 1999 Chi-Chi earthquake rupture, central Taiwan, *J. Geophys. Res.* **116,** no. B7, doi: 10.1029/2010JB007760.

Noguchi, K., Y. Yamanaka, Y. Tanabe, and T. Iwata (2001). Development of the retrieval system of the historical seismogram catalogue by using web technique, *Technical Research Report*, Vol. 7, Earthquake Research Institute, University of Tokyo, 64–71.

Omori, F. (1907). Preliminary note on the Formosa earthquake of March 17, 1906, *Imp. Earthq. Inves. Comm. Bull.* **2,** 53–71.

Sinotech Engineering Consultants, Inc. (1985). Report on regional geological study of Peikang Basement High area and the Meishan Fault, *Taisee Site Feasibility Study*, 160 pp.

Taihoku Meteorological Observatory (TMO) (1911). *Report of the Weather of Taiwan*, 93–97 (in Japanese).

Taihoku Meteorological Observatory (TMO) (1936). *Report of the Severe Hsinchu-Taichung Earthquake of April 21, 1935*, 160 pp.

Taiwan Governor-General Office of Civil Affairs (1907). *Report of Earthquake Damages of Chiayi*, Taipei, 428 pp.

Wells, D. L., and K. J. Coppersmith (1994). New empirical relationships among magnitude, rupture length, rupture width, rupture area, and surface displacement, *Bull. Seismol. Soc. Am.* **84,** no. 4, 974–1002.

Wu, Y.-M., T.-L. Teng, T.-C. Shin, and N.-C. Hsiao (2003). Relationship between peak ground acceleration, peak ground velocity, and intensity in Taiwan, *Bull. Seismol. Soc. Am.* **93,** no. 1, 386–396.

Yeh, Y.-T., M.-T. Hsu, and S.-N. Cheng (1998). *Report of the Rearrangement and Analysis of Ten Disastrous Earthquakes Occurring in Taiwan from 1898 to 1997* (in Chinese).

Yu, S.-B., H.-Y. Chen, and L.-C. Kuo (1997). Velocity field of GPS stations in the Taiwan area, *Tectonophysics* **274,** no. 1, 41–59.

Zhao, L., P. Chen, and T. H. Jordan (2006). Strain Green's tensors, reciprocity, and their applications to seismic source and structure studies, *Bull. Seismol. Soc. Am.* **96,** no. 5, 1753–1763.

***Yi-Wun Liao*[1]**
***Kuo-Fong Ma*[1]**
***Hao Kuo-Chen*[1]**
Earthquake-Disaster & Risk Evaluation and Management (E-DREaM) Center
National Central University
300 Jongda Road, Zhongli District
Taoyuan 32001
Taiwan
fong@earth.ncu.edu.tw

Ming-Che Hsieh
Disaster Prevention Technology Research Center

Sinotech Engineering Consultants, Inc.
280 Xinhu 2nd Road, Neihu District
Taipei 11494
Taiwan

Shi-Nan Cheng
Department of Applied Geomatics
Chien Hsin University of Science and Technology
229 Jianxing Road, Zhongli District
Taoyuan 32097
Taiwan

Chung-Pai Chang
Center for Space and Remote Sensing Research
National Central University
300 Jongda Road, Zhongli District
Taoyuan 32001
Taiwan

Published Online 2 May 2018

[1] Also at Department of Earth Sciences, National Central University, 300 Jongda Road, Zhongli District, Taoyuan 32001, Taiwan.